https://doi.org/10.5194/essd-2025-447
Preprint. Discussion started: 10 September 2025

Open Access Earth System Science Data Discussions

Global Ice Water Path Retrieval Using Fengyun series Satellite Data: A Machine Learning Approach

Yifan Yang[1], Tingfeng Dou[1], Gaojie Xu[1], Rui Zhou[1], Bo Li[2], Letu Husi[3], Wenyu Wang[4], Cunde Xiao[5]

[1]State Key Laboratory of Earth System Numerical Modeling and Application, College of Resources and Environment, University of Chinese Academy of Sciences, Beijing, 101408, China
[2]Innovation Center for Fengyun Meteorological Satellite (FYSIC), Key Laboratory of Radiometric Calibration and Validation for Environmental Satellites, National Satellite Meteorological Center (National Center for Space Weather), China Meteorological Administration, Beijing 100081, China
[3]State Key Laboratory of Remote Sensing and Digital Earth, Aerospace Information Research Institute, Chinese Academy of Sciences, Beijing, 100101, China
[4]Key Laboratory of Microwave Remote Sensing, National Space Science Center, Chinese Academy of Sciences, Beijing 100190, China
[5]State Key Laboratory of Earth Surface Processes and Disaster Risk Reduction, Beijing Normal University, Beijing, 100875, China

Correspondence to: Tingfeng Dou (doutf@ucas.ac.cn)

Abstract. This study presents a novel machine learning framework (RobustResMLP) for retrieving the global ice water path (IWP) and cloud ice water path (CIWP) from 2009-2024 via passive microwave observations from China's Fengyun-3 series satellites' microwave humidity sounders (MWHS-I/II). The framework employs a lightweight multilayer perceptron architecture enhanced with gated residual units and hierarchical differential dropout to address the challenges associated with high-noise satellite data. By establishing rigorous spatiotemporal collocation with CloudSat 2C-ICE products, we generate three operational products: (1) synoptic type that orbital-resolution IWP/CIWP (15 km; 2009-2024), (2) climatic type that gridded monthly composites (1°×1°; 2011-2024), and (3) cloud layer mask (CLM) products. Notably, the 89 GHz channel emerges is the most influential predictor despite theoretical limitations. This approach achieves a critical compromise between pointwise accuracy and spatiotemporal completeness, enabling unprecedented decadal-scale cloud feedback analyses. All the datasets are open available in the netCDF4 format for community sharing.

1 Introduction

The radiative effects of clouds and their feedback processes on global and regional climates are extremely important and complex, making clouds among the most significant sources of uncertainty in climate

https://doi.org/10.5194/essd-2025-447
Preprint. Discussion started: 10 September 2025

modeling and projection studies (IPCC, 2023). One crucial parameter in cloud feedback is the ice water path (IWP), which is defined as the vertical integral of the ice water content (IWC). The ice crystals in the atmosphere, particularly within clouds, exert substantial impacts on the radiation budget of the Earth's system, primarily by modulating the cloud phase, and subsequently influencing the cloud optical thickness (Melia et al., 2016). Climate models exhibit significant discrepancies in IWP simulations, often differing by orders of magnitude, with considerable spatial heterogeneity (Eliasson et al., 2011a; Waliser et al., 2009). This highlights the need for high-quality observational constraints on atmospheric ice (Holl et al., 2014).

From an observational perspective, space-based remote sensing is currently the only means of providing continuous, high-resolution global IWP data. However, remote sensing retrievals are often "ill-posed" (Tarantola, 2005), as the measurements depend on multiple factors, such as the ice particle number concentration, particle size distribution, particle shape parameters, and ambient environmental properties. Despite this, retrieving global IWP data via remote sensing remains essential. Microwave radiation can penetrate dense clouds and interact with ice particles, enabling estimates of ice mass and other bulk properties (Eliasson et al., 2011b; Wu et al., 2008). Moreover, some studies have validated that key parameters pertaining to ice crystals in the atmosphere, such as the particle effective diameter, are highly sensitive to different frequency bands of passive microwaves(Sun and Weng, 2012; Zhao and Weng, 2002). Active remote sensing, which detects backscattered signals from emitted electromagnetic waves, provides vertical profiles of the IWP and may offer greater accuracy than passive instruments. However, active sensors typically have narrow swaths, limiting coverage to near-nadir regions (Delanoë and Hogan, 2010; Hong and Liu, 2015). Therefore, using passive microwave instruments to retrieve the atmospheric ice water content is currently one of the best methods for obtaining large-scale, long-term series of IWP data.

At present, the wavelengths of spaceborne passive microwave instruments are mostly concentrated below 200 GHz. This band is sensitive to large ice particles. Representative instruments include the advanced microwave sounding unit-B (AMSU-B) and the microwave humidity sounder (MHS). The microwave humidity sensors (MWHS-I and MWHS-II) onboard China's Fengyun-3 series satellites have similar wavelength settings (89-190 GHz) and accuracies. Moreover, the Fengyun-3 series satellites have long

https://doi.org/10.5194/essd-2025-447
Preprint. Discussion started: 10 September 2025

time series (2009-2024) and complete orbital coverage via morning satellites (FY-3A, FY-3C, FY-3F), afternoon satellites (FY-3B, FY-3D), and dawn-dusk orbit satellites (FY-3E) (An et al., 2023; Tan et al., 2019; Wang et al., 2022). However, the application of data from the Fengyun series satellites is still not sufficient. Therefore, it is possible to use data from the Fengyun-3 series satellites to retrieve the IWP.

Machine learning methods excel in representing nonlinear relationships. Among these methods, supervised learning stands as a crucial component of machine learning, and is extensively utilized at present. It does not require too many empirical assumptions but directly learns the distribution from the data. Essentially, it fits the target function distribution. The difficulty lies in finding highly accurate ground truth data. In traditional IWP retrieval methods, a large number of empirical assumptions are first needed, and it is also necessary to establish a lookup table database on the basis of very complex scattering models; the process consumes a substantial amount of computational power but has the advantage of strong physical interpretability. For example, Letu et al. (2016, 2020) developed an ice crystal scattering database based on an irregular Voronoi model via a combination of the finite-difference time-domain (FDTD) method, the geometric optimal iterative algorithm (GOIE), and the geometric optimal method (GOM). This database has been used in the official ice cloud products of the Global Change Observation Mission - Climate (GCOM-C) and Himawari-8. Several studies have also applied machine learning methods to the retrieval of IWP. Holl et al. (2014) used infrared data and microwave humidity sounder data to train an artificial neural network (ANN), resulting in the SPARE-ICE product, which provides all-weather (day and night) data. Amell (2021) employed quantile regression neural networks (QRNNs) to retrieve IWPs from geostationary satellite passive observations. Using Himawari-8 infrared observations and CatBoost machine learning, Tana et al. (2025) present the first geostationary-satellite, all-day, high-resolution cloud water path retrieval—outperforming MODIS. Wang et al. (2022) retrieved IWPs via the MWHS on the FY-3B satellite. They used a deep neural network (DNN) for this purpose, considering the impact of MWHS polarization channels at 150 GHz on the results. However, that work did not produce a long-term IWP product, nor did it generate CIWP data.

In this study, a novel machine learning framework (RobustResMLP) is developed on the basis of passive instruments, including the MWHS-I and MWHS-II on the Fengyun-3 series satellites, with 2C-ICE data serving as the ground truth for training. We ultimately obtained orbital IWP data and gridded monthly

https://doi.org/10.5194/essd-2025-447
Preprint. Discussion started: 10 September 2025

92 average IWP data from 2009 to the present. Additionally, on the basis of the cloud mask and cloud phase
93 data from 2B-CLDCLASS data, we extracted the cloud ice content from the IWP for training purposes
94 and consequently obtained cloud IWP (CIWP) data from 2009-2024.

95 **2 Data**

96 **2.1 Passive instrument data**

97 The passive microwave instruments used in this study are the MWHS-I and MWHS-II. The MWHS-I is
98 carried on the first batch of China's second-generation low-orbit meteorological satellites (FY-3A, FY-
99 3B). The MWHS-II is divided into two batches. The first batch is carried on the second batch of China's
100 second-generation low-orbit meteorological satellites (FY-3C, FY-3D), and the second batch is carried
101 on the third batch of these satellites (FY-3E, FY-3F). The MWHS-I has five frequency bands ranging
102 from 150-190 GHz. The MWHS-II represents a significant upgrade from the MWHS-I, increasing the
103 number of channels from 5-15. It also adds oxygen absorption channels near 118.75 GHz and a window
104 at 89 GHz (Wang et al., 2024). The channel settings and basic parameters of the MWHS-I and MWHS-
105 II, as well as the data time spans used for each satellite, are given in Tables S1-S4. Level 1 data were
106 used in this research to support the synergistic observations of cloud and atmospheric parameters.

107 **2.2 Active instrument data**

108 The active instrument data suite encompasses two pivotal products for atmospheric cloud studies: the
109 cloud scenario classification product (2B-CLDCLASS) and the CloudSat and CALIPSO ice cloud
110 property product (2C-ICE). The 2B-CLDCLASS product, derived from CloudSat's cloud profiling radar
111 (CPR), delivers high-precision cloud type classifications through a multidimensional framework
112 integrating hydrometeor vertical/horizontal scales, the CPR-measured maximum radar reflectivity factor
113 (Ze), precipitation indicators, and ancillary datasets, including ECMWF temperature profiles and surface
114 topography (Sassen and Wang, 2008). These criteria enable robust cloud climatology analyses, serving
115 dual roles as an observational truth for cloud detection and as a tool to extract CIWP from the IWP data.
116 Similarly, the 2C-ICE product synergizes CPR radar reflectivity (from the 2B-GEOPROF dataset) with
117 CALIPSO's CALIOP lidar attenuated backscatter at 532 nm to refine ice cloud property retrievals. The
118 CPR captures vertical backscatter profiles at 240 m resolution with a 1.4 km × 1.8 km footprint, whereas
119 the combined radar-lidar approach overcomes the limitations of single-instrument retrievals, yielding

https://doi.org/10.5194/essd-2025-447
Preprint. Discussion started: 10 September 2025

enhanced accuracy in IWC estimates (Deng et al., 2010). In this study, the IWP data from 2C-ICE are used as the truth value, and the cloud classification data from 2B-CLDCLASS are employed to extract CIWP from the IWP data, which are also used as training ground truths.

2 Preprocessing

2.1 Quality control

The level 1 data from the Fengyun series satellites include quality-related flags. For the MWHS-II data, three quality flags are provided: the scan line preprocessing quality flag (QA_Scan_Flag), the channel data integrity quality flag (QA_Ch_Flag), and the observed brightness temperature quality score (QA_Score). QA_Scan_Flag is an integer ranging from 0-12113, where 0 indicates successful preprocessing of the scan line. QA_Ch_Flag is a 16-bit binary code stored as an integer between 0 and 65534, with 0 indicating complete channel data. QA_Score ranges from 0 to 100, with higher values indicating better brightness temperature quality. This study sets the following quality thresholds: QA_Scan_Flag = 0, QA_Ch_Flag = 0, and QA_Score ≥ 90. For the MWHS-I data, the following quality flags are similarly provided: calibration quality flag (cal_qc), pixel quality flag (pixel_qc), and scan line quality flag (scnlin_qc). All three flags are integers ranging from 0-65535. We exclusively select data points where all three flags equal 0.

2.2 Collocations

To meet the requirements of machine learning algorithms, passive instrument observations must be spatiotemporally matched with ground truth data. FY-3D and CloudSat are both afternoon satellites, with FY-3D crossing the equator at 2:00 PM local time and CloudSat at 1:30 PM. Temporal matching is straightforward, with a 15-minute window selected to account for typical convective system time scales. Spatially, multiple 2C-ICE pixels may fall within a single MWHS-II pixel since the latter has a resolution of 15 km, an order of magnitude coarser than 2C-ICE. On the basis of previous studies (Holl et al., 2010; Wang et al., 2022), two criteria are used: (1) at least nine 2C-ICE pixels must lie within 7.5 km of an MWHS-II pixel, and (2) the coefficient of variation (standard deviation divided by the mean) of 2C-ICE pixels within an MWHS-II pixel must be less than 0.6. These criteria ensure sufficient representativeness and stability of 2C-ICE pixels within each MWHS-II pixel. Additionally, owing to the frequent overpasses of polar-orbiting satellites over polar regions, the number of matched points in these areas is

https://doi.org/10.5194/essd-2025-447
Preprint. Discussion started: 10 September 2025

148 disproportionately high. To balance the dataset, matched points in polar regions are randomly removed
149 to achieve a uniform distribution across latitude bands. Finally, a dataset of 807330 matched points is
150 produced, covering the time span from 2019-August 2020. For the MWHS-I pixels, FY-3B is also an
151 afternoon satellite with an ascending node local time of 1:40 PM. Therefore, we use its data from
152 December 2010 to April 2011 and match it with the corresponding 2C-ICE data using the same criteria
153 that were used for MWHS-II. This process results in 144,740 matched points. Both datasets are then split
154 into training and testing sets at an 80:20 ratio. For different satellites, the number of points with IWPs
155 equal to 0 in the training set are appropriately adjusted to ensure a balanced representation. Concurrently,
156 the calibration of the CIWP training dataset is similar to that of the IWP dataset. We employ the method
157 of Li et al. (2012). to extract CIWP data from the IWP data of 2C-ICE, which ultimately yields 710903
158 matched points for the MWHS-II instrument and 93460 matched points for the MWHS-I instrument.

159 **3 Postprocessing**

160 **3.1 Gridding, resampling, and averaging**

161 The orbital IWP products retain a spatiotemporal resolution of 15 km. To facilitate climatological studies,
162 the data are gridded monthly at a 1° × 1° resolution. The orbital products are resampled and averaged
163 onto each grid cell.

164 **4 Methodology**

165 **4.1 IWP retrieval algorithm**

166 To retrieve IWP from passive microwave remote sensing observations, we develop a deep neural network
167 based on a multilayer perceptron (MLP) named RobustResMLP as the fundamental model. The MLP is
168 a highly mature deep learning model that is composed primarily of fully connected networks, and it has
169 the advantages of a simple architecture and resource conservation. The model has a parameter count of
170 9 M, making it a lightweight model. We make several significant improvements to the RobustResMLP,
171 which are detailed as follows:

172 (1) Residual Units with Gating and Learnable Weights: We introduce residual units that incorporate a
173 gating mechanism and learnable residual weights. This helps mitigate the vanishing gradient
174 problem in deep networks.

https://doi.org/10.5194/essd-2025-447
Preprint. Discussion started: 10 September 2025

(2) Lightweight Attention and Adaptive Feature Scaling: We combine lightweight attention mechanisms with adaptive feature scaling within the MLP architecture. This dual optimization enhances the model's ability to capture important features.

(3) Hierarchical Differential Dropout Mechanism: We implement a hierarchical differential dropout mechanism. Specifically, the dropout rate is set at 20% in the input layer and within residual blocks, while it is increased to 30% in the output layer. Additionally, we employ pre-layer normalization (Pre-LN) design to form a multi-level regularization defense, effectively suppressing overfitting.

These technical features collectively form an efficient and robust framework for IWP retrieval. While maintaining high computational efficiency, the model demonstrates excellent modeling capabilities for high-noise, nonlinear satellite observation data. Moreover, because the MWHS-II instruments in the two batches have different window channel settings, we construct a lightweight MLP-based model to map the 166 GHz window region of the second batch of MWHS-II instruments to the 150 GHz channel of the first batch. This allows us to use the already registered dataset for training, saving time and computational resources.

Furthermore, to prepare for the next step of integrating optical instruments for data fusion, we construct a cloud detection model based on the MLP to assess the performance on passive microwave observations. The specific structure of the model is shown in Figure 11.

https://doi.org/10.5194/essd-2025-447
Preprint. Discussion started: 10 September 2025

Open Access Earth System Science Data Discussions

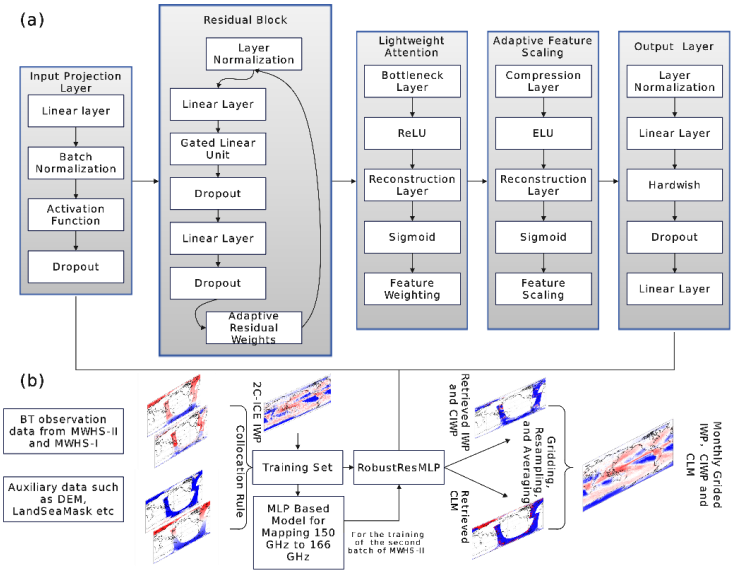

Figure 1: Structural diagram of the RobustResMLP model and flowchart of the retrieval algorithm. (a) Schematic diagram of the RobustResMLP model structure. (b) Flowchart of the IWP product retrieval process.

4.2 Model hyperparameters

The matched training data are split into two parts, one for training (80%) and the other for validation (20%). The IWP ground truth values in the training set are log-transformed, and the IWP values are partitioned into IWP and CIWP values via the 2B-CLDCLASS product. The hyperparameters of the RobustResMLP model are shown in Table 1.

Table 1: Main hyperparameters for the RobustResMLP Model

Module	Hyperparameter	Value
Architecture	Input Dimension	19/14*
	Number of Residual Blocks	8
Regularization	Input Dropout Rate	0.2
	Residual Block Dropout 1	0.2
	Residual Block Dropout 2	0.24
	Output Dropout Rate	0.3
	LayerNorm Epsilon	1.00E-05
Training	Learning Rate	3.00E-04

https://doi.org/10.5194/essd-2025-447
Preprint. Discussion started: 10 September 2025

Open Access Earth System Science Data Discussions

	Weight Decay	0.01
	Batch Size	4096
	Max Epochs	300
	Early Stopping Patience	30
Output Layer	Intermediate Dimension	256
	Output Activation	Hardswish

*19 is the input dimension for MWHS-II, and 14 is the input dimension for MWHS-I.

4.4 Evaluation metrics

The performance of the MLP model in retrieving IWP is evaluated via the root mean square error (RMSE), mean absolute error (MAE), bias (BIAS), and Pearson correlation coefficient (CC), which are calculated as follows:

$$\mathrm{RMSE} = \sqrt{\frac{1}{N}\sum_{i=1}^{N}\left(y_{\mathrm{pred},i} - y_{\mathrm{truth},i}\right)^2} \quad (1)$$

$$\mathrm{BIAS} = \frac{1}{N}\sum_{i=1}^{N}\left(y_{\mathrm{pred},i} - y_{\mathrm{truth},i}\right) \quad (2)$$

$$\mathrm{MAE} = \frac{1}{N}\sum_{i=1}^{N}\left|y_{\mathrm{pred},i} - y_{\mathrm{truth},i}\right| \quad (3)$$

$$\mathrm{CC} = \frac{\frac{1}{N}\sum_{i=1}^{N}\left(y_{\mathrm{pred},i} - \overline{y_{\mathrm{pred}}}\right)\left(y_{\mathrm{truth},i} - \overline{y_{\mathrm{truth}}}\right)}{\sigma_{\mathrm{pred}}\sigma_{\mathrm{truth}}} \quad (4)$$

Here, y_{pred} and y_{truth} represent the model predictions and ground truth, respectively, whereas σ_{pred} and σ_{truth} are the standard deviations.

For cloud detection, performance is evaluated via a confusion matrix M, with metrics including $Accuracy$, $Precision$, $Recall$, and $F1\_score$, defined as:

$$M = \begin{pmatrix} TP & FP \\ FN & TN \end{pmatrix} \quad (5)$$

True positives (TP) correspond to cases where both MWHS and CloudSat detect clouds, whereas true negatives (TN) occur when neither of them identifies cloud presence. False positives (FP) arise when MWHS detects ice clouds that CloudSat does not confirm, and false-negatives (FN) emerge when CloudSat identifies clouds that MWHS fails to detect. This framework establishes MWHS as the test classifier and CloudSat as the validation reference.

$$Accuracy = \frac{(TP + TN)}{(TP + FP + TN + FN)} \quad (6)$$

https://doi.org/10.5194/essd-2025-447
Preprint. Discussion started: 10 September 2025

$$Precision = TP / (TP + FP) \quad (7)$$

$$Recall = TP / (TP + FN) \quad (8)$$

$$F1\_score = 2 * (Precision * Recall) / (Precision + Recall) \quad (9)$$

5 Data records

The file naming convention for the dataset is FY3X_MWHSX_GBAL_L1_YYYYMMDD_HHmm_015KM_MS_iwp.nc, which includes the variables IWP, CIWP, and CLM retrieved from both MWHS-I and MWHS-II. The specific file structure is shown in Figure 2a. The time span of the orbital products ranges from 2009-2024, which is useable for weather-scale studies, such as studies on the mechanisms of precipitation formation and the structure and characteristics of clouds. The data are stored in the netCDF4 file format, with a total of approximately 192880 records. The data size is approximately 606 GB. For climate studies, we provide long-term monthly gridded products (2011-2024) under the naming convention FY3X_MWHSX_GBAL_L1_YYYY_MEAN.nc (structure shown in Figure 2b). The reason for the inconsistency in the time series between the gridded and orbital products is that the IWP values retrieved from the MWHS-I onboard FY-3A showed anomalously low values after gridding, so we excluded them. We further identify and extract the most temporally stable products from the gridded products to construct a homogeneous, long-term dataset for climate studies, which is designated “Merged_Global_Mean.nc”.

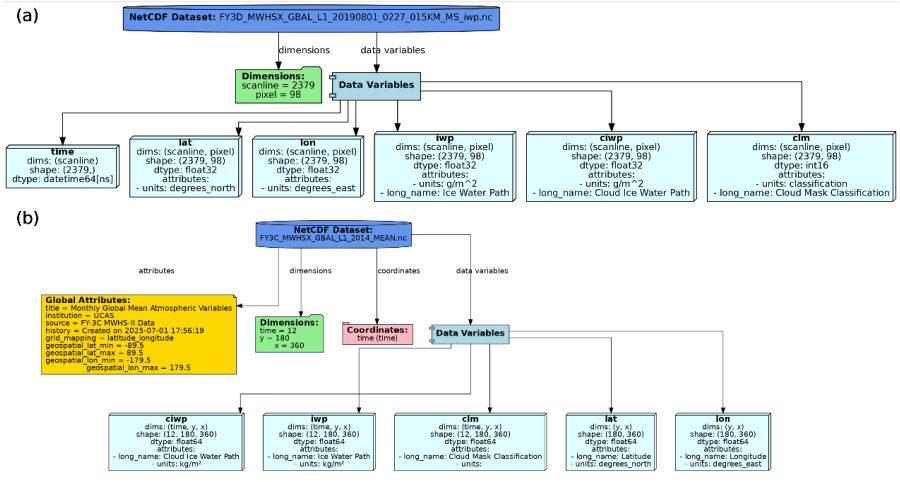

Figure 2: Schematic of the data file structure: (a) orbital data file structure; (b) gridded data file structure.

https://doi.org/10.5194/essd-2025-447
Preprint. Discussion started: 10 September 2025

Open Access Earth System Science Data Discussions

Table 2: Performance of models using different instruments for retrieving the IWP and CIWP

Instrument	variable	RMSE(g/m^2)	BIAS(g/m^2)	MAE(g/m^2)	CC
MWHS-I	IWP	908.13	-167.89	152.92	0.66
	CIWP	189.11	-37.14	68.61	0.64
MWHS-II	IWP	313.39	-24.33	62.50	0.82
	CIWP	190.09	-29.55	67.85	0.76
MWHS-II*	IWP	569.73	-57.44	167.65	0.80
	CIWP	192.85	-33.41	68.96	0.76

* denotes the second-batch MWHS-II instruments onboard the FY-3E/F satellites.

6 Retrieval performance

6.1 IWP retrieval performance

Table 2 demonstrates the performance of the RobustResMLP model for retrieving IWP and CIWP via MWHS-I and MWHS-II data. The results reveal substantial enhancements in the MWHS-II retrievals compared with those of the MWHS-I retrievals, which are primarily attributable to the expanded channel capabilities of the former. Figure 3 comprehensively evaluates model performance: (a) scatter plot of predicted versus true values; (b)-(g) diagnostic analyses of relative errors, absolute errors, and residual distributions. The model delivers high accuracy at low IWP concentrations (<10^3 g/m^2), although errors scale moderately with increasing IWP values. Critically, given the global mean IWP of approximately 100 g/m^2 (Xu et al., 2022), the model maintains robust performance across predominant atmospheric conditions. Table 3 reveals that superior model performance does not necessarily correlate with increased input channels. Our analysis identifies divergent spatial patterns in MWHS-II bands 2-6 observations between the 2019-2020 training data and operational scenarios, inducing anomalously high IWP retrievals. Consequently, we implement a feature selection strategy that excludes bands 2-6 while maintaining competitive accuracy. Additionally, the inclusion of the 89 GHz band significantly enhances the retrieval performance, which is also reflected in its SHAP values (Fig. S1, S2). We conduct a SHAP value analysis of the trained model, and the results reveal that the 89 GHz band ranks first in terms of input feature importance. Although it is not highly sensitive to ice crystals in theory, this finding is consistent with the research of Wang et al. (2024). In terms of auxiliary data selection, we include all the auxiliary data provided by the MWHS L1 data in the training. The results show that it also visibly improves retrieval performance. We further evaluate the retrieval performance separately over ocean/land and day/night regimes, with the results detailed in Table 4.

https://doi.org/10.5194/essd-2025-447
Preprint. Discussion started: 10 September 2025

Open Access Earth System Science Data Discussions

Table 3 Performance of IWP Retrieval Models with Different Input Combinations

Input Channels	Auxiliaries	RMSE(g/m^2)	BIAS(g/ m^2)	MAE(g/ m^2)	CC
9-15	/	918.63	-311.42	311.44	0.12
1, 10, 11, 13, 15	/	870.88	-298.94	298.95	0.16
7-15	/	650.54	-158.85	198.32	0.67
1-15	SolarAzimuth, SolarZenith, DEM, SensorAzimuth, SensorZenith, LandCover, LandSeaMask, lon, lat	482.06	-48.95	149.47	0.81
1, 7-15	SolarAzimuth, SolarZenith, DEM, SensorAzimuth, SensorZenith, LandCover, LandSeaMask, lon, lat	313.39	-24.33	62.50	0.82

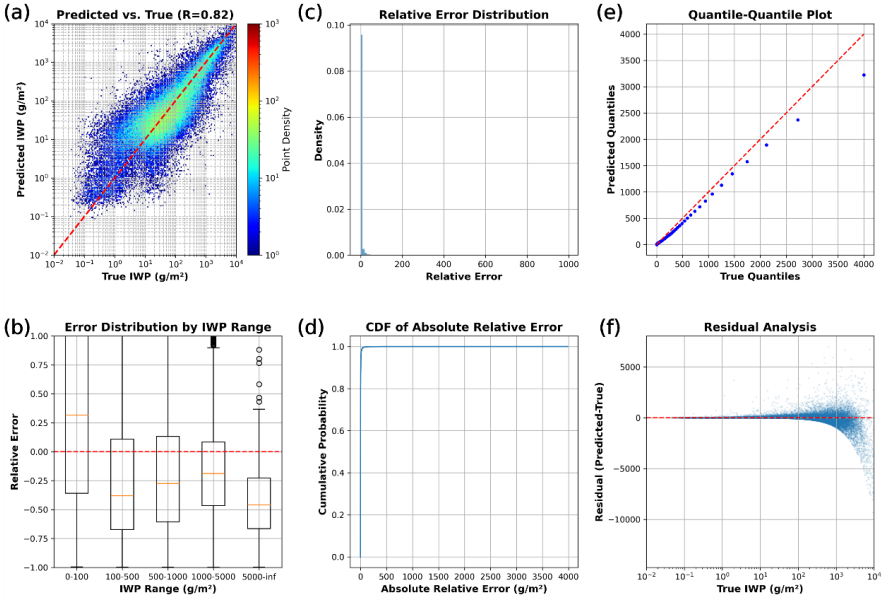

Figure 3: Performance metrics of the RobustResMLP model on the IWP test dataset. (a) Scatter plot of mode-retrieved IWP values versus true values on MWHS-II; (b) box plot of the relative error distribution across different IWP ranges; (c) probability density distribution of the relative errors; (d) cumulative density curve of the absolute errors; (e) QQ plot of predicted values versus true values; (f) scatter plot of the residual distribution.

https://doi.org/10.5194/essd-2025-447
Preprint. Discussion started: 10 September 2025

Table 4: Performance of the RobustResMLP model on Land and Ocean Test Datasets in IWP Retrieval (using the MWHS-II instrument).

	Land	Ocean	Daytime	Nighttime
RMSE(g/m^2)	337.12	294.38	421.3	99.71
BIAS(g/m^2)	-27.56	-21.86	-41.03	-5.74
MAE(g/m^2)	60.48	62.44	105.87	14.21
CC	0.77	0.84	0.80	0.89

6.2 Cloud detection retrieval performance

The cloud detection retrieval performance of RobustResMLP on the test set is shown in Table 5. In terms of performance, MWHS-II shows a significant improvement over MWHS-I. Since this is a preliminary study for the next step, we did not conduct sensitivity experiments on input features but directly used input features similar to those of the IWP model for training.

Table 5: The performance of the cloud detection model on the test datasets (using the MWHS-I instrument).

Instrument	Condition	Precision	Recall	F1-score	Accuracy
MWHS-I	Clear	0.77	0.82	0.79	0.77
	Cloudy	0.76	0.71	0.73	
MWHS-II	Clear	0.94	0.97	0.95	0.92
	Cloudy	0.76	0.6	0.67	

7 Product validation

Four scenarios were used to validate the orbital IWP and annual global gridded IWP products against other datasets.

7.1 Typhoon events

Figure 4 displays orbital IWP retrievals from the MWHS-IWP product, as well as IWP from the 2C-ICE product and the ERA5 reanalysis dataset during Typhoon Wutip in 2019 and Typhoon Soulik in 2013. The IWPs retrieved from both MWHS-I and MWHS-II can accurately capture the high-IWP regions in the typhoon area, which is consistent with the 2C-ICE data. In contrast, while the ERA5 reanalysis data can also roughly reproduce the high-IWP regions, the level of detail is significantly less than that of the retrieval products.

https://doi.org/10.5194/essd-2025-447
Preprint. Discussion started: 10 September 2025

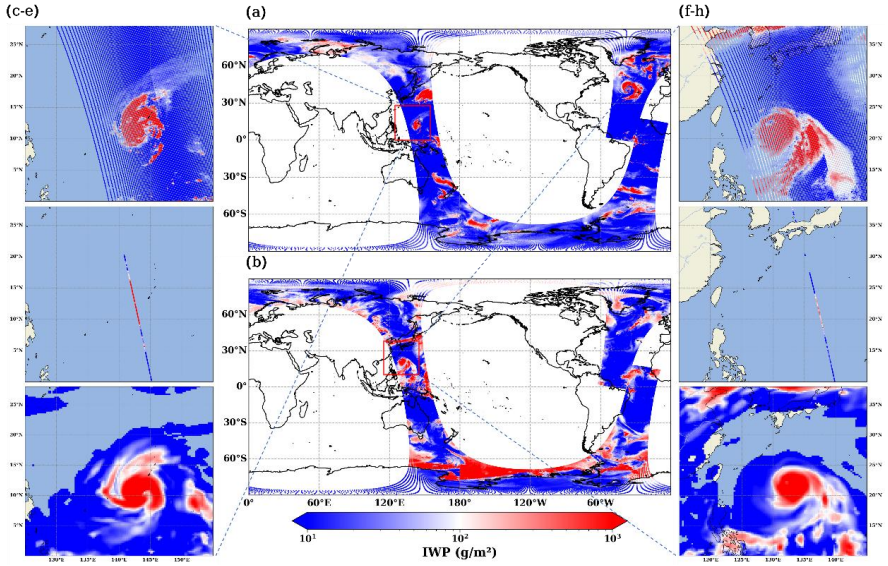

Figure 4: Orbital IWP products during typhoon passage: (a) and (b) show the IWP products retrieved from MWHS-II and MWHS-I, respectively, during the passages of Typhoon Wutip in 2019 and Typhoon Soulik in 2013. (c) is the zoomed-in IWP product retrieved from MWHS-II, which focuses on the area affected by the typhoon. (d) shows the IWP data from the 2C-ICE for the same period. (e) is the IWP product from the ERA5 reanalysis for the same period. (f) is the zoomed-in IWP product retrieved from MWHS-I, which focuses on the area affected by the typhoon. (g) and (h) are the same as (d) and (e), respectively, but for the period coinciding with Typhoon Soulik.

7.2 Global gridded product comparison and zonal mean comparison

Figure 5 presents the multiyear average spatial distribution of the IWP, whereas Figure 6 shows the zonal mean distribution of the IWP. All the IWP products were resampled to a spatial resolution of (1°×1°). All the IWP products exhibit fundamentally consistent spatial patterns. Notably, our product demonstrates closer alignment with active sensor products (particularly the MWHS-II retrieval product). Although the time series do not overlap, we selected the 2007-2010 period for active instrument comparison because of CloudSat's superior data completeness before 2011. This selection is necessitated by data constraints but remains scientifically justified, as both spatial patterns and total magnitudes show minimal variation in long-term IWP sequences. Additionally, passive optical/infrared instruments (MODIS, VIIRS) and the ERA5 reanalysis result in significant underestimations of IWP values at low-to-mid latitudes, whereas the MODIS and VIIRS retrieval products result in substantial overestimations in polar regions. We must also note an anomalous high-value bias in the MWHS-I-based products across southern mid-high latitudes. Further analysis reveals that these elevated values stem not only from a systematic high bias in

https://doi.org/10.5194/essd-2025-447
Preprint. Discussion started: 10 September 2025

317 the dataset but also from an anomalous summertime peak over the Filchner-Ronne ice shelf and Antarctic
318 Peninsula during July and August each year; the precise physical mechanism remains to be elucidated.
319 We address this limitation in future iterations of our retrieval product. For the CIWP, the multiyear
320 average spatial distribution is shown in Fig. S3, the overall distribution closely resembles that of IWP,
321 but the values are lower in magnitude.

https://doi.org/10.5194/essd-2025-447
Preprint. Discussion started: 10 September 2025

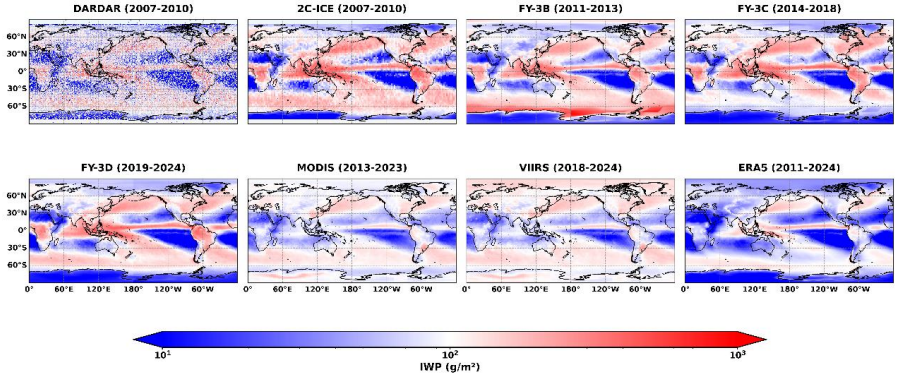

Figure 5: Global average spatial distributions of the IWP compared with those of other satellite products and reanalysis products.

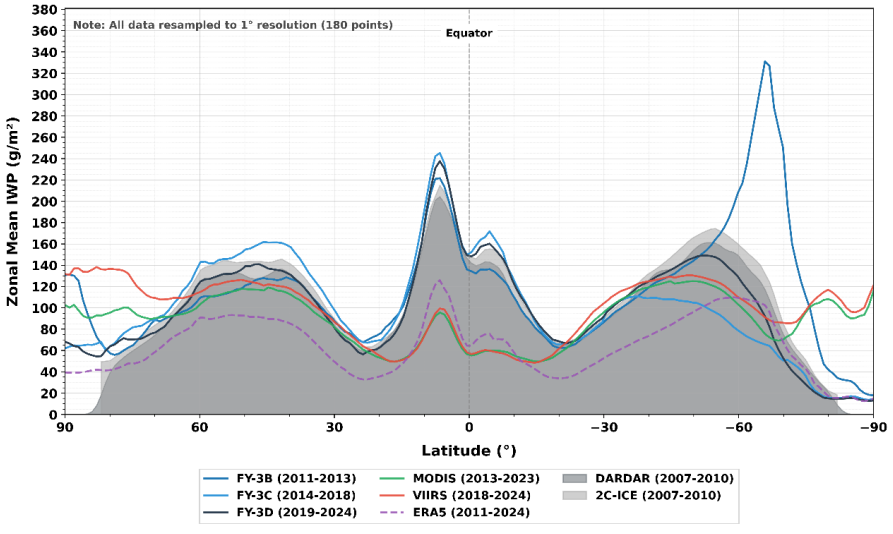

Figure 6: Zonal mean IWP compared with other satellite products and the ERA5 reanalysis.

7.3 Long-term analysis of gridded products

Figure 7 shows the global total atmospheric ice mass curve from the gridded retrieval products for the period of 2011-2024. The orange and blue-green lines represent the IWP data from 2C-ICE and DARDAR (another IWP product based on active remote sensing instruments (Melia et al., 2016)), respectively. Owing to battery issues with CloudSat after 2011, which led to the loss of nighttime data, the time series for the 2C-ICE and DARDAR products are restricted to 2007-2010. Our retrieval products are closer to 2C-ICE and DARDAR in terms of the total global atmospheric ice mass. In contrast, the atmospheric ice totals calculated from the passive optical/infrared instruments MODIS and VIIRS, as

https://doi.org/10.5194/essd-2025-447
Preprint. Discussion started: 10 September 2025

well as the ERA5 reanalysis data, are significantly lower than those from 2C-ICE and DARDAR IWP. All calculations are weighted by latitudinal area. The global total atmospheric ice mass from our retrieval products for the period 2011-2024 is 58.66 (58.20, 59.12) Gt, which is close to our previous estimation using the DARDAR product (Xu et al., 2022). For the CIWP, the long-term global total mass is shown in Fig. S4.

https://doi.org/10.5194/essd-2025-447
Preprint. Discussion started: 10 September 2025

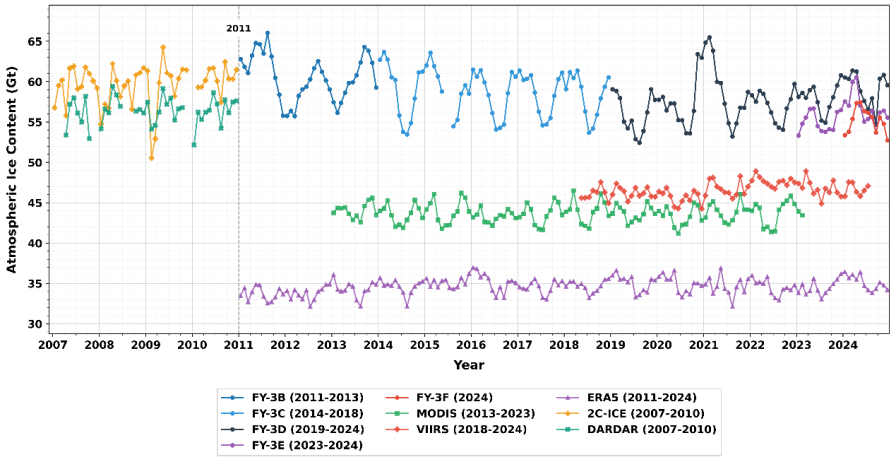

Figure 7: Native time series of the monthly global average of total atmospheric ice and comparison with other satellite products, along with the ERA5 reanalysis. All calculations of total atmospheric ice consider latitude area weighting.

8 Conclusion and usage notes

This study developed a machine learning framework to retrieve global IWPs and CIWPs from 2009-2024 via passive microwave observations from the MWHS-I and MWHS-II aboard the Fengyun-3 series satellites.

Three distinct IWP products were generated:

(1) Orbital-level IWP and CIWP products preserving native sensor resolutions (15 km), with a time series from 2009-2024.

(2) Monthly gridded global composites (1° × 1°) from individual sensors, with a time series from 2011-2024.

(3) CLM products were generated for both instruments.

While the retrieval accuracy of neural networks may not surpass that of benchmark products such as 2C-ICE under optimal observational conditions, their superior spatial sampling (enabling complete global coverage within orbital swaths) and temporal continuity (maintaining consistent retrieval performance across sensor generations) make them particularly valuable for decadal-scale climate variability analysis. This trade-off between pointwise accuracy and spatiotemporal completeness represents a strategic

https://doi.org/10.5194/essd-2025-447
Preprint. Discussion started: 10 September 2025

compromise that aligns with the requirements of climate system monitoring, where long-term homogeneity often takes precedence over instantaneous retrieval precision.

We generated two sets of retrieval products. The orbital products include the IWP, CIWP, and cloud layer mask (CLM) retrieved via FY-3A (2008-2014), FY-3B (2010-2019), FY-3C (2013-2024), FY-3D (2019-2024), FY-3E (2022-2024), and FY-3F (2023-2024). These methods can be used for synoptic scale studies, such as studies of cloud structure and precipitation mechanisms. Notably, our products achieved global coverage over both oceanic and land regions, whereas most passive microwave-based IWP retrievals are limited to oceanic regions. Furthermore, our incorporation of CIWP retrievals represents a distinctive advancement rarely available in international equivalent products. However, if long-term trends are investigated, we recommend the use of our gridded products, which provide comprehensive coverage from 2011-2024. If gridded products are created using our orbital data, please avoid using data from FY-3A, FY-3B after 2017, and FY-3C after 2019. Owing to potential instrument aging, the retrieved IWP values during these periods may sometimes be anomalously high. While this does not significantly affect weather-scale studies, it can impact long-term trend analyses.

While this study demonstrates the feasibility of IWP retrieval via passive microwave instruments, several limitations warrant further investigation. Passive microwave instruments are actually more sensitive to liquid droplets, and are theoretically sensitive only to large ice crystals (especially snowflakes), so they typically overlook some cirrus clouds. Future work will explore advanced data fusion architectures, including (1) joint retrievals using optical/infrared remote sensing instruments, which are sensitive to cloud-top information and can be used to compensate for the lack of sensitivity to cirrus clouds in passive microwave instruments; (2) joint retrieval frameworks that simultaneously assimilate multispectral observations within a unified radiative transfer model; and (3) physics-informed neural networks incorporating cloud microphysical constraints to improve vertical stratification accuracy.

Current orbital products lack sub-daily temporal resolutions. To address this limitation, forthcoming research will incorporate FY-4A/B geostationary observations with 15-minute temporal resolutions. Parallel to this integration, continuous upgrades and maintenance of existing datasets are being implemented. Furthermore, we have noted rapid advancements in terahertz remote sensing

https://doi.org/10.5194/essd-2025-447
Preprint. Discussion started: 10 September 2025

instrumentation (Li et al., 2023). We will actively monitor these developments and subsequently employ terahertz technology to achieve higher-accuracy retrievals of IWP and CIWP. Collectively, these enhancements significantly increase the product's utility for monitoring rapidly evolving meteorological phenomena and validating climate model cloud parameterizations.

9 Code and data availability

Data from the Fengyun-3 series satellites' MWHS-I/II Level-1 observations are accessible via the NSMC data portal (https://data.nsmc.org.cn). CloudSat-CALIOPSO products (2C-ICE and 2B-CLDCLASS) are available through the CloudSat data processing center (https://www.cloudsat.cira.colostate.edu). Generated datasets from this study may be cited as https://doi.org/10.11888/Atmos.tpdc.302932 and https://cstr.cn/18406.11.Atmos.tpdc.302932 (Yang et al., 2025) , with the processing codes available upon request to the corresponding author. Besides, the code used to create the figures in this paper, including code for generating the figures and pre- and post-processing the data, is available at https://doi.org/10.5281/zenodo.16352115 (Yang, 2025).

Author contributions. YFY conceived the main algorithm, produced the dataset, validated its accuracy, and drafted the manuscript. GJX and RZ also contributed to parts of the algorithm design. BL, LTHS, WYW, CDX, and TFD supervised data production and validation, and revised the manuscript.

Competing interests. The contact author has declared that none of the authors has any competing interests.

Disclaimer. Publisher’s note: Copernicus Publications remains neutral with regard to jurisdictional claims in published maps and institutional affiliations.

Acknowledgements. The authors acknowledge the National Satellite Meteorological Center (NSMC) and CloudSat Data Processing Center for providing access to the satellite data utilized in this work.

Financial support. This research is supported by National Natural Science Foundation of China grant 42222608.

https://doi.org/10.5194/essd-2025-447
Preprint. Discussion started: 10 September 2025

419 **Reference**

420 Amell, A.: Geostationary passive retrieval of ice water path with quantile regression neural networks,
421 CHALMERS UNIVERSITY OF TECHNOLOGY, Gothenburg, Sweden, 2021.

422 An, N., Shang, H., Lesi, W., Ri, X., Shi, C., Tana, G., Bao, Y., Zheng, Z., Xu, N., Chen, L., Zhang,
423 P., Ye, L., and Letu, H.: A Cloud Detection Algorithm for Early Morning Observations From the
424 FY-3E Satellite, IEEE Trans. Geosci. Remote Sens., 61, 1–15,
425 https://doi.org/10.1109/TGRS.2023.3304985, 2023.

426 Delanoë, J. and Hogan, R. J.: Combined CloudSat-CALIPSO-MODIS retrievals of the properties
427 of ice clouds, J. Geophys. Res. Atmospheres, 115, 2009JD012346,
428 https://doi.org/10.1029/2009JD012346, 2010.

429 Deng, M., Mace, G. G., Wang, Z., and Okamoto, H.: Tropical Composition, Cloud and Climate
430 Coupling Experiment validation for cirrus cloud profiling retrieval using CloudSat radar and
431 CALIPSO lidar, J. Geophys. Res. Atmospheres, 115, 2009JD013104,
432 https://doi.org/10.1029/2009JD013104, 2010.

433 Eliasson, S., Buehler, S. A., Milz, M., Eriksson, P., and John, V. O.: Assessing observed and
434 modelled spatial distributions of ice water path using satellite data, Atmospheric Chem. Phys., 11,
435 375–391, https://doi.org/10.5194/acp-11-375-2011, 2011a.

436 Eliasson, S., Buehler, S. A., Milz, M., Eriksson, P., and John, V. O.: Assessing observed and
437 modelled spatial distributions of ice water path using satellite data, Atmospheric Chem. Phys., 11,
438 375–391, https://doi.org/10.5194/acp-11-375-2011, 2011b.

439 Holl, G., Buehler, S. A., Rydberg, B., and Jiménez, C.: Collocating satellite-based radar and
440 radiometer measurements – methodology and usage examples, Atmospheric Meas. Tech., 3, 693–
441 708, https://doi.org/10.5194/amt-3-693-2010, 2010.

442 Holl, G., Eliasson, S., Mendrok, J., and Buehler, S. A.: SPARE-ICE: Synergistic ice water path from
443 passive operational sensors, J. Geophys. Res. Atmospheres, 119, 1504–1523,
444 https://doi.org/10.1002/2013JD020759, 2014.

445 Hong, Y. and Liu, G.: The Characteristics of Ice Cloud Properties Derived from CloudSat and
446 CALIPSO Measurements, J. Clim., 28, 3880–3901, https://doi.org/10.1175/JCLI-D-14-00666.1,
447 2015.

448 IPCC: Climate Change 2021 – The Physical Science Basis: Working Group I Contribution to the
449 Sixth Assessment Report of the Intergovernmental Panel on Climate Change, Cambridge University
450 Press, Cambridge, https://doi.org/10.1017/9781009157896, 2023.

451 Letu, H., Ishimoto, H., Riedi, J., Nakajima, T. Y., C.-Labonnote, L., Baran, A. J., Nagao, T. M., and
452 Sekiguchi, M.: Investigation of ice particle habits to be used for ice cloud remote sensingfor the
453 GCOM-C satellite mission, Atmospheric Chem. Phys., 16, 12287–12303,
454 https://doi.org/10.5194/acp-16-12287-2016, 2016.

https://doi.org/10.5194/essd-2025-447
Preprint. Discussion started: 10 September 2025

455 Letu, H., Yang, K., Nakajima, T. Y., Ishimoto, H., Nagao, T. M., Riedi, J., Baran, A. J., Ma, R.,
456 Wang, T., Shang, H., Khatri, P., Chen, L., Shi, C., and Shi, J.: High-resolution retrieval of cloud
457 microphysical properties and surface solar radiation using Himawari-8/AHI next-generation
458 geostationary satellite, Remote Sens. Environ., 239, 111583,
459 https://doi.org/10.1016/j.rse.2019.111583, 2020.

460 Li, J. -L. F., Waliser, D. E., Chen, W. -T., Guan, B., Kubar, T., Stephens, G., Ma, H. -Y., Deng, M.,
461 Donner, L., Seman, C., and Horowitz, L.: An observationally based evaluation of cloud ice water in
462 CMIP3 and CMIP5 GCMs and contemporary reanalyses using contemporary satellite data, J.
463 Geophys. Res. Atmospheres, 117, 2012JD017640, https://doi.org/10.1029/2012JD017640, 2012.

464 Li, M., Letu, H., Ishimoto, H., Li, S., Liu, L., Nakajima, T. Y., Ji, D., Shang, H., and Shi, C.:
465 Retrieval of terahertz ice cloud properties from airborne measurements based on the irregularly
466 shaped Voronoi ice scattering models, Atmospheric Meas. Tech., 16, 331–353,
467 https://doi.org/10.5194/amt-16-331-2023, 2023.

468 Melia, N., Haines, K., and Hawkins, E.: Sea ice decline and 21st century trans-Arctic shipping routes:
469 Trans-Arctic shipping in the 21st Century, Geophys. Res. Lett., 43, 9720–9728,
470 https://doi.org/10.1002/2016GL069315, 2016.

471 Sassen, K. and Wang, Z.: Classifying clouds around the globe with the CloudSat radar: 1-year of
472 results, Geophys. Res. Lett., 35, 2007GL032591, https://doi.org/10.1029/2007GL032591, 2008.

473 Sun, N. and Weng, F.: Retrieval of Cloud Ice Water Path from Special Sensor Microwave
474 Imager/Sounder (SSMIS), J. Appl. Meteorol. Climatol., 51, 366–379,
475 https://doi.org/10.1175/JAMC-D-11-021.1, 2012.

476 Tan, Z., Ma, S., Zhao, X., Yan, W., and Lu, W.: Evaluation of Cloud Top Height Retrievals from
477 China's Next-Generation Geostationary Meteorological Satellite FY-4A, J. Meteorol. Res., 33,
478 553–562, https://doi.org/10.1007/s13351-019-8123-0, 2019.

479 Tana, G., Lesi, W., Shang, H., Xu, J., Ji, D., Shi, J., Letu, H., and Shi, C.: A New Cloud Water Path
480 Retrieval Method Based on Geostationary Satellite Infrared Measurements, IEEE Trans. Geosci.
481 Remote Sens., 63, 1–10, https://doi.org/10.1109/TGRS.2025.3526262, 2025.

482 Tarantola, A.: Inverse Problem Theory and Methods for Model Parameter Estimation, Society for
483 Industrial and Applied Mathematics, https://doi.org/10.1137/1.9780898717921, 2005.

484 Waliser, D. E., Li, J. F., Woods, C. P., Austin, R. T., Bacmeister, J., Chern, J., Del Genio, A., Jiang,
485 J. H., Kuang, Z., Meng, H., Minnis, P., Platnick, S., Rossow, W. B., Stephens, G. L., Sun-Mack, S.,
486 Tao, W., Tompkins, A. M., Vane, D. G., Walker, C., and Wu, D.: Cloud ice: A climate model
487 challenge with signs and expectations of progress, J. Geophys. Res. Atmospheres, 114,
488 2008JD010015, https://doi.org/10.1029/2008JD010015, 2009.

489 Wang, W., Wang, Z., He, Q., and Zhang, L.: Retrieval of ice water path from the Microwave
490 Humidity Sounder (MWHS) aboard FengYun-3B (FY-3B) satellite polarimetric measurements
491 based on a deep neural network, Atmospheric Meas. Tech., 15, 6489–6506,

https://doi.org/10.5194/essd-2025-447
Preprint. Discussion started: 10 September 2025

492 https://doi.org/10.5194/amt-15-6489-2022, 2022.

493 Wu, D. L., Jiang, J. H., Read, W. G., Austin, R. T., Davis, C. P., Lambert, A., Stephens, G. L., Vane,
494 D. G., and Waters, J. W.: Validation of the Aura MLS cloud ice water content measurements, J.
495 Geophys. Res. Atmospheres, 113, 2007JD008931, https://doi.org/10.1029/2007JD008931, 2008.

496 Xu G., Dou T., Yang Y., Yue H., Letu H., Ma L., and Xiao C.: The total mass and spatio-temporal
497 structure of the aerial cryosphere, Chin. Sci. Bull., 67, 4130–4139, https://doi.org/10.1360/TB-
498 2022-0184, 2022.

499 Yang, Y.: Global Ice Water Path Retrieval Using Fengyun series Satellite Data: A Machine
500 Learning Approach/generating figures and pre-post- precessing code, ,
501 https://doi.org/10.5281/zenodo.16352116, 2025.

502 Yang, Y., Dou, T., Zhou, R., Li, B., Husi, L., Wang, W., and Xiao, C.: Fengyun polar-orbiting
503 satellite total/cloud ice water path retrieval dataset (2009-2024). National Tibetan Plateau / Third
504 Pole Environment Data Center, https://doi.org/10.11888/Atmos.tpdc.302932., 2025.

505 Zhao, L. and Weng, F.: Retrieval of Ice Cloud Parameters Using the Advanced Microwave
506 Sounding Unit, J. Appl. Meteorol., 41, 384–395, https://doi.org/10.1175/1520-
507 0450(2002)041<0384:ROICPU>2.0.CO;2, 2002.

508